

BUNCH-RESOLVED DIAGNOSTICS FOR A FUTURE ELECTRON-STORAGE RING

G. Schiwietz, J.-G. Hwang, A. Jankowiak, M. Koopmans, M. Ries*

**Helmholtz-Zentrum Berlin für Materialien und Energie GmbH,
Albert-Einstein-Str. 15, 12489, Berlin, Germany**

Abstract:

The upgrade of the BESSY II light source in Berlin towards a variable pulse-length storage-ring will lead to a complex bunch-filling pattern. This may involve co-existing electron bunches with significant variations of their properties. Among many other conditions, it calls for bunch-resolved diagnostics with sub-ps time resolution and micrometer spatial resolution. Currently, we are finishing the constructing of a diagnostic platform connected to new dipole beamlines for visible light as well as THz measurements. The mid-term aim is 24/7 use of optical beam diagnostics and the development of advanced methods for specific purposes. Preliminary interferometric data for transverse beam profiles are presented and discussed. The main topic of this paper, however, are recent streak-camera results along with concepts to achieve high signal-to-noise ratio, high time resolution and 2D diagnostics at high efficiency.

PACS: **41.85.Qg** - Particle beam analyzers, beam monitors, and Faraday cups
 29.27.Fh - Beam characteristics
 84.30.Sk - Pulse and digital circuits

Keywords: **Electron-beam diagnostics, non-destructive measurements, bunch-selectivity, 2D diagnostics, high-resolution streak-camera system**

* contact: schiwietz@helmholtz-berlin.de

1. TRANSITION FROM BESSY II TO BESSY-VSR

The current BESSY II electron-storage ring of the Helmholtz-Zentrum Berlin (HZB) is operated at the energy of 1.7 GeV with a cavity frequency of 500 MHz. The maximum ring current is 300 mA. Different electron optical modes are available and various bunch-filling patterns are distributed within 400 RF buckets that are separated by approximately 2 ns.

The envisioned long-term upgrade towards the Variable pulse-length Storage-Ring (BESSY VSR [1-3]) involves a triple-cavity structure at high electric field strengths. Thus, the bunch length will be reduced significantly at fixed charge values, see Fig. 1. This means that time-dependent X-ray experiments (coincidences, pump/probe measurements, etc.) will gain time resolution, whereas precision spectroscopy and scattering experiments running in parallel will profit from stable and large mean currents.

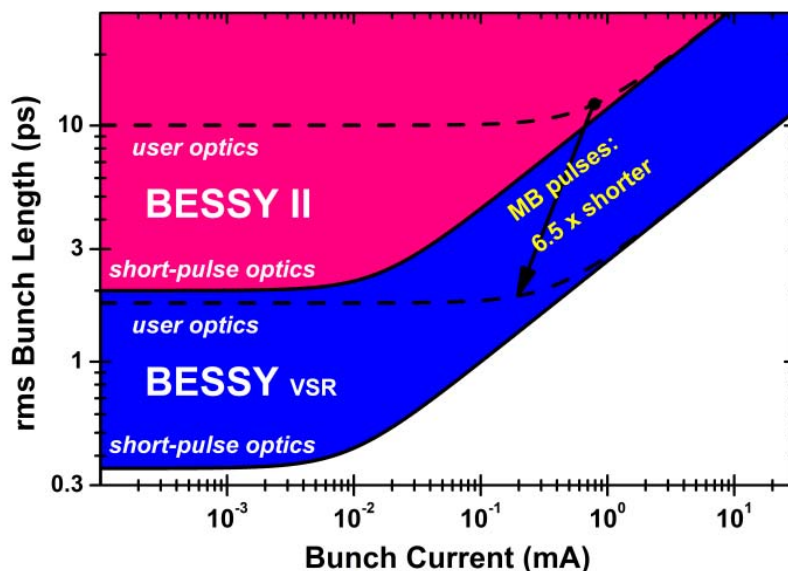


Fig. 1. Comparison of standard user optics as well as short-pulse optics for BESSY II with the future BESSY VSR system, considering realistic SRF boundary conditions.

Superposition of the 500 MHz normal conducting cavity with additional 1.5 GHz and finally also 1.75 GHz provided by SRF (superconducting RF) at high voltages would lead to a beating pattern of the RF field gradients and corresponding formation of alternating short and long buckets every 2.0 ns. This is the basis of a complex fill pattern with co-existing bunches that differ regarding bunch length, bunch charge, transverse profile and charge density.

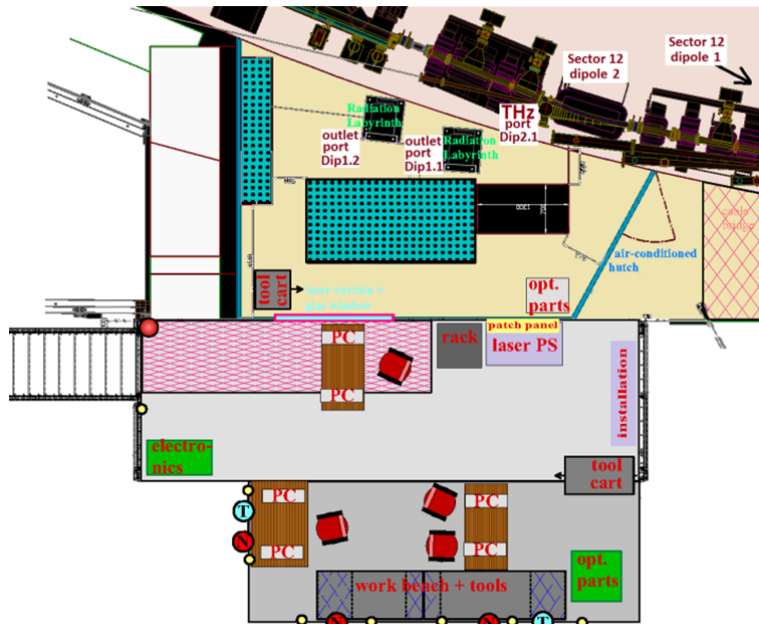
Control of a complex fill pattern calls for new and improved capabilities of beam-diagnostics hardware. Consequently, for the bunch-resolved longitudinal beam diagnostics (bunch length and phase), we have recently set up a sub-ps streak camera [4] at a new diagnostic dipole beamline. Further, we are considering and testing other innovative methods for this purpose [5] as well. Diagnostics of the lateral beam size and position variation are performed using direct imaging as well as double-slit and π -polarization interferometry [6,7] of visible light. For these optical beam-diagnostics tools, high sensitivity and high resolution are required for the large bunch-to-bunch variations in BESSY II [8] and BESSY VSR [1-3] with good signal-to-noise ratio.

2. BUNCH-RESOLVED OPTICAL DIAGNOSTICS

2.1. New platform and beamlines

The design target of the new diagnostic systems includes robustness, sufficient space for R&D and 24/7 availability. The new diagnostic platform features visible-light output ports from two dipole beamlines (see Fig. 2) of the BESSY II storage ring. In each case, X-ray blocking baffles avoid excessive heat loads on the subsequent mirrors. The absorbed synchrotron power on the mirrors is below 3 W and the use of thermally stabilized mirror substrates with water cooling system minimizes wave-front distortions. Depending on the beamline two or three mirrors are installed inside an evacu-

33 ated beamline to reduce the influence of dust and air humidity on the light transport. At the outlet of each evacuated
 34 line, the light passes through a radiation labyrinth and exits into air through a wedged glass window.



35
 36 **Fig. 2.** Scheme of the new Diagnostic Platform, showing the three outlet ports and the main installations.
 37

38 One dipole beamline (*Sector12-Dip1.2* in Fig. 2) is dedicated to lateral size and beam-halo measurements. This beam-
 39 line is optimized for good wave-front propagation, involving moderate source-opening angles. The extracted light will
 40 be transmitted from this beamline to an optical table, mainly for the future bunch-resolved interferometric transverse-
 41 size monitor (see also subsection 2.2). The Sector12-Dip1.2 beamline will be equipped with 3 custom-made precision
 42 planar mirrors (active area of 70x70 mm², manufactured by Pilz-Optics, Germany) optimized for temperature stability.
 43 Inspection of these mirrors by our optics department has shown minimum radial curvatures of >35 km and measured
 44 slope errors below 0.4 arc sec. [9] These parameters should enable excellent wave-front propagation in the beamline up
 45 to the optical table.

46 The primary mirror M1 is placed behind an adjustable X-ray blocking baffle yielding a shadowed angular range of
 47 0.736 mrad in the vertical direction. M1 is temperature stabilized by a water-cooling system. It reflects photons from
 48 the electron-beam tunnel upward in the direction of a radiation labyrinth on the upper floor. Inside the concrete structure
 49 of the labyrinth, a second mirror M2 reflects the light back into the horizontal plane. M1 and M2 are motor controlled
 50 since there is no direct mechanical access to the radiation-safety area. On the working height of the optical table,
 51 the light leaves the evacuated part of the beamline through a wedged outlet window (type VPCF100DUVQ-L-WEDGE0.5,
 52 by VACOM, Germany) with 98 mm open-area diameter and planarity < $\lambda/4$.

53 Downstream, a 3rd plane mirror, M3, provides coupling onto the optical table. At this point, the maximum opening
 54 angles are 6.1 mrad horizontally x 4.3 mrad vertically, if no focusing is applied by inserting a motorized 2.4" achro-
 55 matic lens at a position between M1 and M2. There is also a motor-controlled selection of different interference targets
 56 that may be inserted directly after the lens. These interference targets are also used for the optical Interferometric Beam-
 57 Size Monitor (IBSM) discussed in the next subsection. The interference target plus lens provides small beam-diameter
 58 resolution and enhanced photon densities (in comparison to our previous configuration).

59 For standard operation of the IBSM [4, 10-12], most optical elements are placed on an optical table. These elements
 60 are

- 61 • a standard double-slit target,
- 62 • a polarizer,
- 63 • two achromatic focusing lenses,
- 64 • optical bandpass filter,
- 65 • an image-detection system (see the next subsection).

66 The use of an optical table outside the radiation tunnel will also allow for a comparison of direct spot imaging, dou-
 67 ble-slit interferometry [10-15] and the X-ray baffle method with pi-polarized light [6,13,16] for vertical beam-size

68 measurements. Currently it seems, however, that double-slit interferometry is the most flexible method covering beam
69 sizes between 11 and 160 μm . Furthermore, it is applicable for both lateral directions.

70 Another beamline (*Sector12-Dip1.1* in Fig. 2) uses a second port from the same dipole. This beamline is optimized
71 for high photon yield, with a large source-opening angle of $20 \times 3.5 \text{ mrad}^2$ (limited by the central X-ray baffle and M1).
72 It mainly consists of a primary focusing mirror M1, an intermediate focal point with adjustable aperture and a subse-
73 quent toroidal mirror M2 yielding a collimated visible light beam that is filtered and guided to the streak-camera en-
74 trance-optics.

75 The primary mirror M1 is a custom-made cooled precision ellipsoidal focusing mirror (hexapod controlled), with
76 slope errors below 2 arcsec rms and a surface roughness below 0.25 nm rms (manufactured by Carl Zeiss Laser Optics
77 GmbH, Germany). Although these parameters are state-of-the-art for production of such an elliptical mirror [9], the
78 slope errors determine the overall quality of light-transport to the streak camera [17] as quantified in the appendix.

79 The collimating mirror M2 is motor-controlled, but not water cooled as the synchrotron-radiation power at this point
80 is just a few mW. This precision toroidal mirror, with slope errors below 1.3 arcsec rms and a surface roughness below
81 0.4 nm rms (custom product manufactured by WinlightX, France), replaces a temporary toroid that was combined with
82 a defocusing cylindrical lens to yield a virtual beam not far from the collimation condition. If not indicated otherwise,
83 all data and results presented in this paper have been obtained with that temporary solution.

84 This beamline is used for electron-beam diagnostics since January 2019 and then upgraded with an improved toroidal
85 mirror, new extraction stage with wedged window, polarizer and flexible periscope optics. Between mirror M2 and the
86 streak-camera the beam passes through

- 87 • a standard wedged vacuum-exit window,
- 88 • an adjustable polarizer,
- 89 • two filter wheels with various band-pass filters (not used for the regular streak-camera measurements),
- 90 • 3 thin beam splitters (for light extraction to other equipment) and
- 91 • 7 high quality plane visible-light mirrors (type 34-398, protected silver coating, by Edmund Optics) with
92 high quality ($\lambda/20$) and 50 mm diameter, for light transport at the diffraction limit [9,17].

93 A system of 7 irises simplifies adjustment of the synchrotron light along the reference-beam path defined by an
94 alignment laser. Together with an adjustable aperture at the intermediate focal point and a fixed aperture at the wedged
95 output window, the aperture system suppresses stray light from inside the vacuum tubes and from scattering at imper-
96 fections close to mirror edges. It also suppresses backscattered light from other optical elements on the optical table.
97 These high-quality mirrors, anti-reflection coatings, intermediate focal point, rectangular apertures and circular dia-
98 phragms, result in suppression of halo structures and light reflections and lead to a good signal-to-noise ratio for the
99 streak camera. In order to confirm this statement, we have compared the projected intensity of the streak camera image
100 with the standard BESSY-II bunch-filling monitor. This indicates linear bunch-charge dependence and a dynamic range
101 exceeding 3 orders of magnitude for the streak camera, similar to the bunch-filling monitor that is limited by counting
102 statistics. The dynamic range of the streak camera seems to be determined mainly by noise from multiple scattering of
103 synchrotron light in the tunnel.

104 At 15 m after the dipole source point, the collimated light is focused by an achromatic lens. This lens produces a focal
105 spot in the mirror-based entrance optics of the streak camera. At this point, the light passes through a vertical collimator
106 slit to limit the spot in the slow-scan direction as well as through a horizontal precision slit to limit the vertical spot size,
107 and is transferred to the cathode of the streak camera.

108 Both optical tables (one for lateral bunch-size, one for bunch-length measurements) rest on air damped legs to reduce
109 ground vibrations. Slow motion of an optical table yields a blurring of the focus. This produces an apparent beam-size
110 increase for slow detectors and intensity fluctuations for fast detectors, e.g., streak cameras. Previously, such vibrations
111 have limited the maximum CCD integration time to <4 ms for our interferometric beam-size determinations (using rigid
112 legs for the same optical table at our previous beam line).

113 We have performed absolute frequency-dependent vibration measurements on our optical table for longitudinal
114 measurements with and without air damped legs. From these measurements, we observe that the upper frequency
115 boundary of the main vibration component (with integrated displacements in the 10- μm range) is reduced from 50 Hz
116 down to about 12 Hz. Other vibration bands with much smaller displacements stay either constant or also show a re-
117 duced bandwidth. Thus, detector integration times may be increased from 3 ms to about 15 ms, without risking a signif-
118 icant vibration blurring of spots. After leaning on the optical table, it returns to the standard position within about 2
119 seconds and after more than one year of operation, we did not recognize a significant change of the table height.

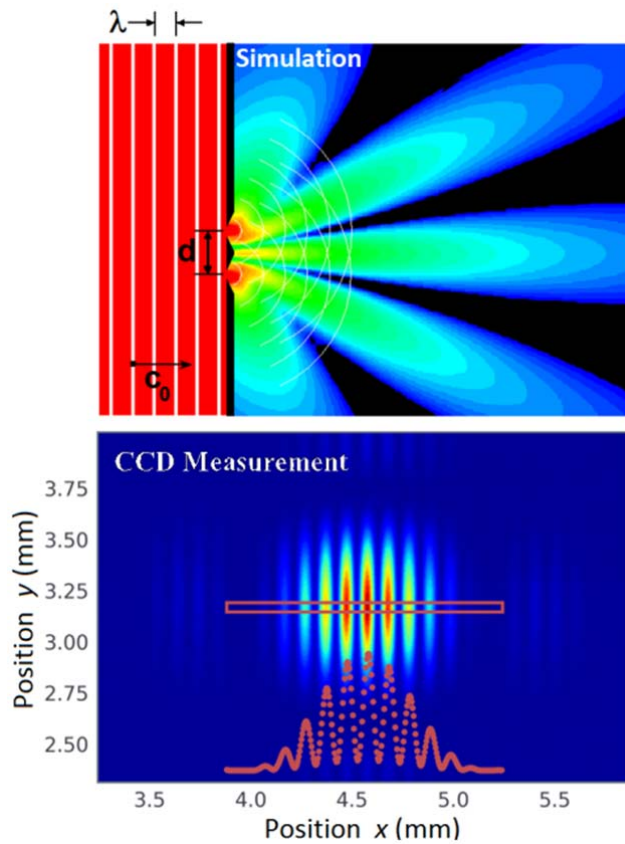
120 During spring 2020, both optical tables have been encased by an air-conditioned hutch against the influence of dust,
121 external sound and unwanted stray light in the experimental hall. Additional space is available outside the hutch for
122 computer controls, signal processing, workbenches and storage.

123 A third dipole beamline (*Sector12-Dip2.1* in Fig. 2) will be placed inside the BESSY II electron-ring tunnel about 2
124 m above the ring level, for reducing radiation damage inside the detector system. This beamline is intended exclusively
125 for THz intensity measurements and spectral THz investigations. From these measurements, the stability of the electron

126 beam can be monitored on different time scales. Nowadays, detectors are fast enough to enable bunch selectivity. Short-
 127 time fluctuations or bursting, e.g., will show up in the THz spectrum, independent of the timing-trigger system (see
 128 section 3.2 for trigger-free bunch-length measurements).
 129

130 **2.2. Transverse beam size: interferometry**

131 A review of beam-diagnostics methods to determine averaged transverse bunch properties has been given by G. Kube
 132 [13]. A more specific review on the principles of double-slit interferometry for visible light has been presented by T.
 133 Mitsuhashi [14]. This method enables accurate transverse beam-size determination by analysis of the interference pat-
 134 tern behind a double slit at a fixed distance from the source point. For more than two years, our version of the IBSM has
 135 demonstrated robustness and reliability [4,10-12,18]. Typical raw data from these preparatory investigations are shown



136 in Fig. 3.

137
 138 **Fig. 3.** Visible-light interferometry of the lateral electron-beam distribution. The upper plot shows a calculated dou-
 139 ble-slit interference-pattern. The lower plot displays a 2D-pattern taken at our diagnostics test beamline for a standard
 140 exposure time of 1 ms. The dotted red curve is a projection of this pattern within the region of interest (solid red rectan-
 141 gle).
 142

143 An appropriate double-slit separation yields a clear interference pattern in the CCD camera, which shifts as a function
 144 of the source-point position. Thus, a broad distribution of incoherent emitters (source points) leads to smearing out of
 145 the interference pattern. Specifically the destructive minima are very sensitive to the smearing effect and the beam-size
 146 determination relies on a fit to the measured pattern. Investigations of different properties of mean bunch sizes have
 147 been performed with this setup using CCD camera detection including

- 148 • measurements of normal and excited bunch structures in both lateral directions in comparison to pinhole re-
 149 sults [10-12,18-19],
- 150 • rotation-angle dependent IBSM measurements of the projected beam size [11, 12] that yield the lateral 2D
 151 distribution (see also similar data and tomography-type evaluation in refs. [20,21]),
- 152 • determination of the absolute resolution of the IBSM by using beam-loss monitors [18],

- evaluation of uncertainties entering precision of the IBSM by exploring different properties such as wavelength, band-pass width, polarization, double-slit structure (see also [22] for beam-profile reconstruction via inverse Fourier transform), differential photon yield, and camera exposure times [10-12].

Compared to the existing BESSY II X-ray pinhole systems [19], our IBSM leads to a significantly improved source-size resolution (11 μm vs. 27 μm) [18]. Further, the IBSM works also at lower electron-beam energies, where pinhole monitors (with fixed X-ray absorber) fail. The IBSM resolution is influenced mainly by the distance between bending magnet and double slit, the quality of the light-transport system and mechanical vibrations. The compromise between small statistical errors and small vibration effects has led to optimal CCD illumination times of 0.5 ms for high light intensity and about 3 ms for low intensity. Thus, most experiments have been performed for an exposure time of 1 ms (at $\lambda=400\text{nm}$, σ -polarization, and double-slit distance of 20 mm), as seen in Fig. 3. For horizontal-size measurements, incoherent depth-of-field effects have to be considered, specifically for small beam sizes of a few μm [11, 15].

An upgraded version of the IBSM is currently being set up at the new diagnostic beamline at *Sector12-Dip1.2*. The new interferometry beamline, as described in section 2.1, shall start operation by the beginning of year 2021. Here, we have tried to reduce all sources of errors that were identified at the original IBSM setup.

The vacuum part of this beamline will involve an optical relay system with high quality motorized mirrors and a motorized X-ray blocking baffle (reduction of wave-front errors), reduced influence of ground vibrations as well as an additional interference stage. This retractable interference stage will be at a reduced distance from the bending-magnet source-region, enabling an improved resolution for small beam sizes. All these measures should further improve the position resolution and robustness of the measurement.

An Intensified CCD camera with fast gating (ICCD camera type XXRapidFrame by Stanford Computer Optics) will enable bunch-resolved interferometry for transverse beam profiling with minimum exposure times of 200 ps. The low ICCD timing jitter of 10 ps rms (including adjustable delay), however, calls for an improved accuracy of the BESSY revolution trigger described in section 2.5. The camera will typically operate for exposure times of 300 ps, gated every 800 ns (every turn of the ring). This enables bunch-selective measurements averaged over multiple turns. The exposure of the gated CCD detector for an individual bunch will last for about 15 ms averaging over about 19000 turns, before mechanical vibration may reduce the image quality (see section 2.1).

In comparison to our previous time-averaged CCD measurements, we will acquire data for an extended illumination time (x15) with improved optical quality (x2). With an improved obstacle design (x2) and at lower detection noise by using microchannel plate magnification (x2), we also gain compared to the previous setup. However, bunch-selective data is acquired only for 1 out of 300 populated bunches per turn. Thus, we expect a similar quality as achieved for Fig. 3 with our previous setup. An additional simulation of the expected interference pattern accounting for the measured light power and different source of noise has verified that the final performance will be good enough for bunch-resolved interferometry. This is consistent with experimental data of this type that have recently been obtained for intermediate time resolutions of about 2 to 3 ns [23,24].

2.3. Bunch length: high time resolution and 2D streak-camera modes

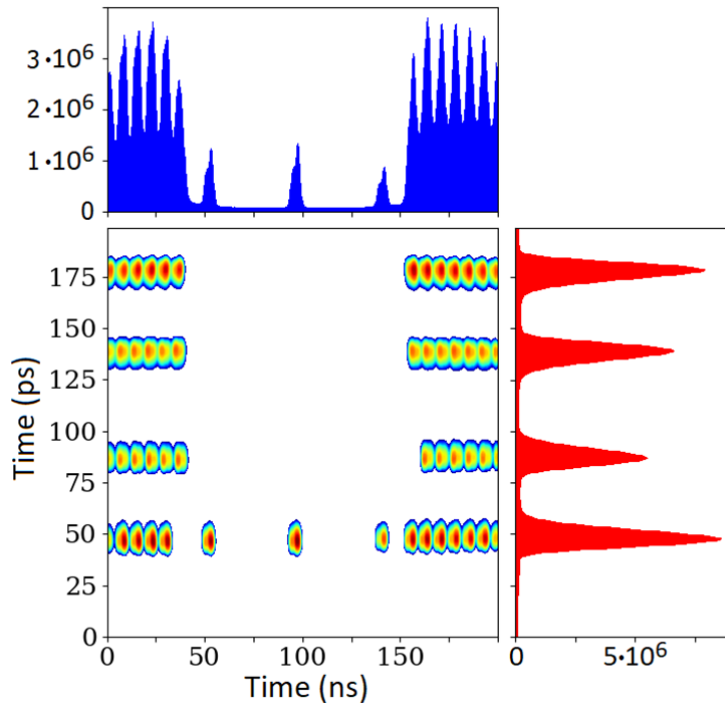
The new diagnostic beamline *Sector12-Dip1.1* for timing investigations is in full in operation. The transfer-optical elements enable selection of polarization, wavelength, bandwidth, and include periscope optics for an exchange of the transversal light-beam axes on the optical table. Measurements with a fast streak-camera (FSC) and also geometrical beam imaging of larger profiles as well as interferometry of the vertical beam size by using the X-ray baffle method with pi-polarized light [6,16] are possible. During the write-up of this paper, this beamline has been optimized (new toroidal mirror M2, additional collimation systems, new RF dividers, further motorization, etc.) and thus, some of the results discussed here are preliminary to a certain extent. A quantitative comparison of the properties of our system with other well-established 2D-streak camera systems is presented in the appendix.

The FSC (type HAMAMATSU C10910-05) involves an exceptionally high repetition rate of 1 kHz for the horizontal scan, a unique design modification initiated by our diagnostic project. The FSC single-shot time resolution derived from a commissioning experiment with a fs-laser beam at our laboratory is 0.88 ± 0.18 ps FWHM ($\sigma\approx 0.37$ ps rms), after consideration of external sources of timing jitter [4]. For time-average measurements extending over some minutes, we reach an all-over time resolution of about 1.5 ps FWHM under standard operating conditions (see appendix). This value is mainly influenced by the wavelength dispersion of optical elements, but also by the remaining trigger jitter and slightly by the local thickness variation of the wedged vacuum window. Reducing the number of beam splitters in the optical path and blocking the synchrotron light at short wavelengths should reduce the total time resolution to 1.1 ps FWHM.

The FSC involves a vertical scanning frequency of 125 MHz derived from the 500-MHz ring RF (divided by 4). Thus, only every second bunch can be detected directly (either even or odd bunch positions of the fill pattern). Using a beam splitter and a delay stage (Newport M-IMS800LM) in a Michelson configuration, pulses from the other fraction (e.g., odd bunch positions) are delayed by about 2 ns to become visible in the FSC. With this FSC double-pulse mode, we can investigate bunch trains without any gap in the detection sequence. The stable frequency of the BESSY-II bunch-fill pattern yields the calibration of the slow scan axis and the precision delay table (typical repeatability = 0.2

211 μm FWHM) is used to calibrate the fast time axis with an accuracy on the fs scale (limited by the electronic timing
 212 jitter, see section 2.5). For each axis, a 3rd order polynomial is fitted to measured peak centers and used to correct the
 213 time scales.

214 Results of the FSC double-pulse configuration are displayed in Fig. 4, for the BESSY II low- α mode at a total ring
 215 current slightly below 15 mA. At the horizontal time axis (slow sweep) below 50 ns and above 150 ns, one may see four
 216 rows with the multi-bunch train, where each consecutive bunch is filled with a similar charge (the real time difference is
 217 2 ns). Some specific bunches [8] appear only in the lower row (discussed further below). Two of the four rows represent
 218 the direct signal from the upward sweep plus the downward sweep of the (fast) vertical FSC time axis (bunch number
 219 $1+4n$ and $3+4n$). The FSC double-pulse method leads to the other two rows for bunch numbers $2+4n$ and $4+4n$. Thus,
 220 we are able to investigate all bunches in parallel.



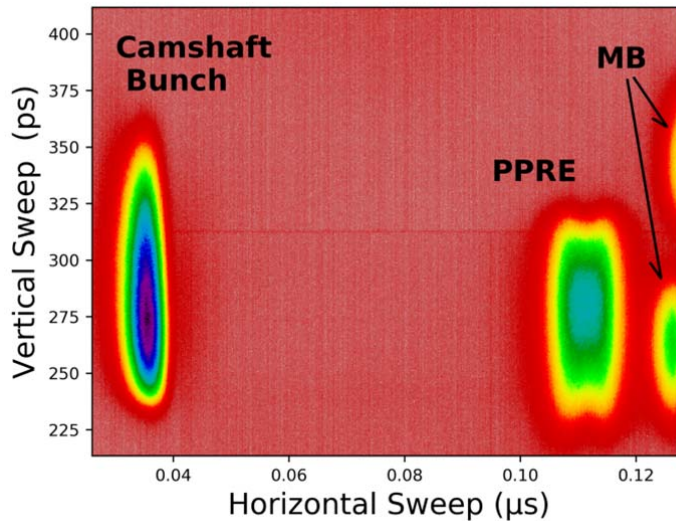
221
 222 **Fig. 4.** FSC raw data of the BESSY II low- α mode for the central 200 ns out of 800 ns bunch-fill pattern.
 223

224 The distance between neighboring bunches inside each row is 8 ns, allowing for encoding of additional information
 225 along the slow-scan axis. Note that the bunch length of about 10 ps FWHM in Fig. 4 (vertical extent) corresponds to
 226 only 0.06 pixels in the horizontal direction. This means that the slow-scan axis (horizontal streak direction) is largely
 227 decoupled from the fast-scan axis (vertical streak direction).

228 The FSC beamline and transfer optics are optimized for high quality time and image resolution at a light-path length
 229 of 15.5 m from the dipole source to the FSC cathode. Optical beam-profile measurements have been performed at dif-
 230 ferent distances and analyzed with simulations from the ray-tracing program RAY-UI [17]. The horizontal entrance slit
 231 of the FSC, typically 13 μm , cuts a narrow horizontal slice out of the 2-dimensional focal spot and this determines the
 232 time-resolution limit. When the additional FSC collimation aperture in the horizontal direction is wide open, lateral
 233 position and size information are encoded in the horizontal streak-camera patterns along the slow-scan axis. As the
 234 vertical bunch shape along the fast-scan axis contains the time information, we are able to measure bunch-resolved 2D
 235 information (t vs. x or t vs. y). For closely spaced bunches, i.e., within the multi-bunch train, peak structures may over-
 236 lap in the horizontal streak-camera direction due to the intrinsic resolution given by the Abbe limit, aberrations, the
 237 point-spread function and the encoded transversal-size information. The peak smearing and blending is counteracted by
 238 selecting a low time range for the horizontal scan axis (about 100 ns in Fig. 5), to increase the horizontal bunch separa-
 239 tion in the image.

240 Dependent on the chosen configuration of the transfer-line mirrors (periscope optics), we may acquire either horizon-
 241 tal or vertical beam shapes vs. the time distribution of each spot (see, e.g., refs. [25-29] for non-destructive 2D analy-
 242 sis). The third parameter (the other transversal direction) may in principle be scanned sequentially using a motor-
 243 controlled mirror. It is noted that a bunch- and turn-selective data acquisition of both transversal directions (without

244 bunch-length information) is also possible with an ICCD camera [25]. Even three-parameter detection (2 times 2D) is in
 245 principle possible for pure single-bunch operation [26, 27, 29], but currently not intended (see also appendix for a de-
 246 tailed comparison with other 2D streak systems).
 247



248 **Fig. 5.** FSC measurement, showing full 2D shapes including the variation of the bunch-lengths and horizontal-size
 249 for different types of electron bunches. Analog integration of the incoming light has been performed for a few seconds
 250 at high optical beamline transmission (no filters, no beam splitters).
 251
 252

253 A 2D measurement is shown as an example in Fig. 5. Data have been taken in the analog FSC integration mode for
 254 the standard BESSY II user fill-pattern [8] during top-up operation. The plot shows the center of this standard bunch-fill
 255 pattern with 3 different types of BESSY II bunches

- 256 • The camshaft bunch (with 4mA bunch current) is placed at the center of the pseudo-single-bunch gap. It serves
 257 for ps-pump/probe absorption and scattering experiments as well as for electron time-of-flight measurements
 258 in combination with a high-speed mechanical chopper [30] or electron analysis with a time sensitive retarding
 259 Bessel-box spectrometer [31,32].
- 260 • The PPRE bunch (bunch current 3mA) for Pulse Picking by Resonant Excitation [33] serves as a pseudo-
 261 single bunch for time dependent experiments at a few BESSY II beamlines. Here, a specific electron bunch is
 262 modified by a quasi-resonant incoherent excitation close to the first synchrotron side band [34]. Finally, a frac-
 263 tion of this broadened electron bunch is separated from all other stored bunches simply by asymmetric collima-
 264 tion of the X-rays produced by an undulator.
- 265 • Two bunches of the Multi-Bunch train (MB) are visible on the right-hand side of Fig. 5 (see also Fig. 4). About
 266 300 of these low-charge bunches (with currents of 0.9 mA per bunch) dominate the BESSY II fill pattern and
 267 the total ring current. For most experiments, they constitute a quasi-dc current, but at the so-called MAXY-
 268 MUS beamline, time resolved MB detection and analysis is performed [35,36].
 269

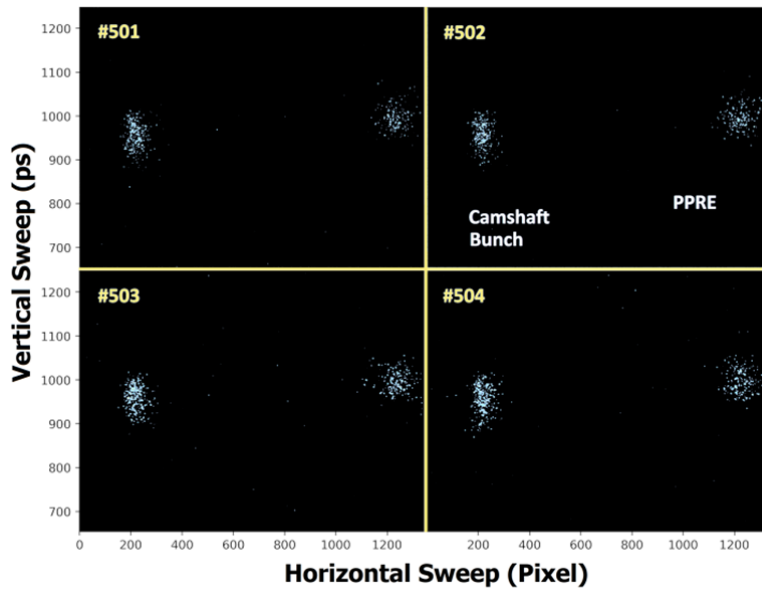
270 One can see that each vertical spot size on the FSC image (corresponding to the bunch length) in Fig. 5 depends sig-
 271 nificantly on the bunch charge. Furthermore, the horizontal peak width shows also a clear bunch characteristic. The
 272 PPRE bunch appears to be horizontally much wider than all other bunches (this will be quantified below). However, it
 273 is not trivial to distinguish between an intrinsic bunch broadening and/or a position fluctuation of the PPRE bunch, if
 274 such a fluctuation is small. Thus, we have derived a statistical analysis method to resolve bunch fluctuations in any
 275 direction.

276 2.4. Statistical snapshot analysis of 2D streak-camera images

277 The PPRE method for producing a quasi-single-bunch signal is mainly applied to time-resolved photoemission stud-
 278 ies under ps-pump/probe conditions [33]. For satisfactory user operation, however, there should be a steady pulse of
 279 photons every turn from this bunch, without beating or varying intensity. Thus, one has to check that the spatial width
 280 of the electron bunch is large compared to its position fluctuation. A new snapshot-analysis method that allows for a
 281 distinction between steady-state broadening and turn-by-turn fluctuations is introduced in the following.

282
283
284
285
286
287
288
289

Fig. 6 shows 4 single-shot images out of 1000 stored images, taken in the analog acquisition mode without camera-pixel binning at a triggered frame rate of about 59 Hz. These 1000 images are statistically analyzed in this subsection. The BESSY-II electron ring was running at standard user top-up conditions at a total electron current of 250 mA. These data have been taken at lower light intensity (reduced by about a factor of 1/800), in order to avoid image saturation for the high-current bunches and to yield a countable number of individual photon hits. Light transmission/reflection at multiple beam splitters and passage through a 10-nm bandpass filter centered at 500 nm was used for intensity reduction.



290
291
292
293
294
295

Fig. 6. Four adjacent FSC images (numbers 501 to 504) taken from a series of 1000 single-shot images, measured at reduced light intensity to avoid saturation effects. Each image represents a single turn for the camshaft bunch and for the PPRE bunch. The images show blobs (with different radii) corresponding to individual detected photon hits. Non-linear contrast enhancement has been applied for better visibility of the data.

296
297
298
299
300
301
302
303

The individual photon strikes shown in Fig. 6 involve a strong variation of their intensity, typical for single Micro-Channel-Plate (MCP) image intensifiers (see, e.g., refs. [37,38]). Furthermore, the radii of the corresponding blobs vary between about 1.5 and 4.5 pixels prohibiting a unique solution for deconvolution. This prohibits also exact counting of overlapped hits. Analysis of the four cases in Fig. 6 indicates mean per-shot photon-numbers of $N_{ph}(CS) = 219 \pm 5$ and $N_{ph}(PPRE) = 162 \pm 3$ for the camshaft bunch and for the PPRE bunch, respectively. The uncertainties of the photon numbers are not statistical errors, but relate to differences in repeated manual counting and computer-aided counting methods. Note that the background due to noise blobs within the region of interest corresponds to only three counts and is already considered in the stated numbers.

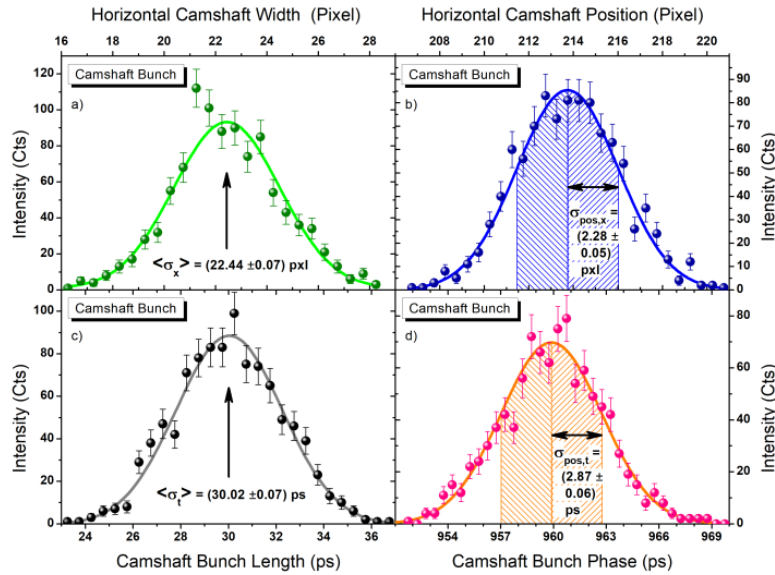
304
305
306
307
308
309
310
311

The ratio $N_{ph}(CS)/N_{ph}(PPRE)$ agrees well with the bunch current ratio determined from the intensities measured by the BESSY bunch fill-pattern monitor. Furthermore, the total number of photons is consistent with the photon flux estimated from the light power, the mean photon energy, the fractional bunch current, the revolution frequency, the relay-line transmission, the FSC entrance-slit intensity-reduction as well as the light-conversion efficiency of the cathode and the MCP open-area ratio. If the whole MCP would see a spatial photon density similar to the camshaft and PPRE bunch centers in Fig. 6, it would correspond to a total photon count-rate of about 1 million cps at a trigger frequency of 59 Hz. This is a reasonable number for a single MCP detector, but it might lead to significant count-rate saturation in double MCP (Chevron type) photon-counting detectors [31,38,39] as part of streak cameras or other setups.

312
313
314
315
316
317
318

For all acquired FSC images, as displayed in Fig. 6, a fixed region of interest (ROI) around the camshaft bunch, respectively around the PPRE bunch, has been defined. For a specific bunch, the light intensity inside the ROI is projected onto the two directions and binning of these primary raw data is performed. Direct statistical evaluation of the variance or standard deviation has been tested. For some images, however, even single photon blobs (related to noise events far away from the center of the distribution) yield a significant influence on these results. As an alternative, we applied least-square fitting to the histograms with Gaussian distributions. Such fits are mainly sensitive to the main peak regions and yield stable results, nearly insensitive to noise.

319 In total, we have extracted 1000 values for each of the 8 parameters of a single image (width and position for 2 bunch
 320 types and for the two directions). The evaluated images include the four cases shown in Fig. 6. A closer look at the time
 321 sequences of these eight parameters reveals a statistical fluctuation around the mean parameter values, without obvious
 322 correlations.
 323



324
 325 **Fig. 7.** Statistical evaluation of 1000 single-shot acquisitions (1000 individual turns) of the camshaft bunch regarding
 326 spot center and spot width in two dimensions (longitudinal and horizontal electron-beam directions).
 327

328 Figures 7 and 8 display 4 histogram plots corresponding to the 1000 single-turn single-bunch images. For this repre-
 329 sentation, binning has been performed. Fig. 7 contains the horizontal width and position as well as bunch length (longi-
 330 tudinal width) and bunch phase (related to the longitudinal position) for the camshaft bunch. Fig. 8 contains the same
 331 information for the PPRE bunch.

332 It can be seen the data in Fig. 7 are well described by Gaussian curves. This indicates a pure statistical nature of the
 333 distributions. Below, we will analyze the statistical relation between width and accuracy of the position information on
 334 a quantitative basis, accounting for different effects related to a realistic counting scenario considering MCP signal
 335 amplification. Except for quantitative differences, the data for the PPRE bunch (in Fig. 8) look similar to the camshaft
 336 bunch (in Fig. 7). Only one of the data sets shows a slight deviation from the fitted Gaussian curve. The horizontal
 337 PPRE position data set (plot b in Fig. 8) drops off slightly faster than the Gaussian curve at both outer wings. This
 338 might be an indication for a non-statistical behavior, i.e., an influence of physical fluctuations of the bunch-center posi-
 339 tion. Systematic effects such as synchrotron oscillations are less likely, because they are expected to appear also for the
 340 camshaft bunch. In the quantitative treatment for the horizontal coordinate, we recognize a clear non-statistical compo-
 341 nent, as will be shown in the following.
 342

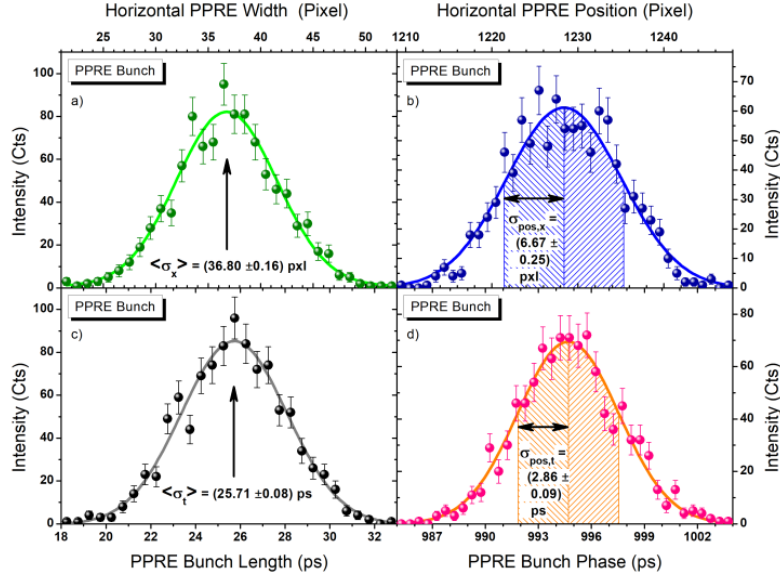


Fig. 8. Statistical evaluation of 1000 single-shot acquisitions of the PPRE bunch regarding spot center and spot width in both dimensions (longitudinal and horizontal electron-beam directions).

Before we analyze Figs. 7 and 8, we discuss the expected relation between the statistical parameters in a simple manner. We then present Monte-Carlo simulations that include a treatment close to the real measurement conditions. Pure linear counting effects do not mix the different statistical parameters along different directions. Thus, we may consider each direction (t for time and x for the horizontal beam coordinate) separately.

If we assume a constant signal distribution along a coordinate d (d stands for t or x or y), the characteristic width is σ_d , the standard deviation. The simplest type of signal is a binary count or no count. Now we consider an event with a fixed number N_d of binary counts. If N_d is infinite, then the mean position p_d is fixed with arbitrary accuracy. In other words, the standard deviation of the position fluctuations is $\sigma_{\text{pos},d} = 0$. If $N_d = 1$ (just one signal per event) then the mean position fluctuates strongly and we have $\sigma_{\text{pos},d} = \sigma_d$. For a large but finite number of signals per event, the uncertainty of the mean position per event drops with the square root of N_d , a fact well known from theory of statistics.

In the following, we will consider effects beyond simple binary signals of a given signal number N_d . We make use of the fact that the 2D distribution contains a given number of signals for each event, not depending on the projected coordinate. Thus,

$$N_d = N_t = N_x = N_{ph} \quad (1)$$

where N_{ph} is the detected number of photons within the ROI. If one considers a factor c that corrects for deviations from the oversimplified counting statistics, the square-root dependence discussed above may be rewritten as

$$\sigma_{\text{pos},d} = \langle \sigma_d \rangle / \sqrt{c \cdot N_{ph}} \quad (2)$$

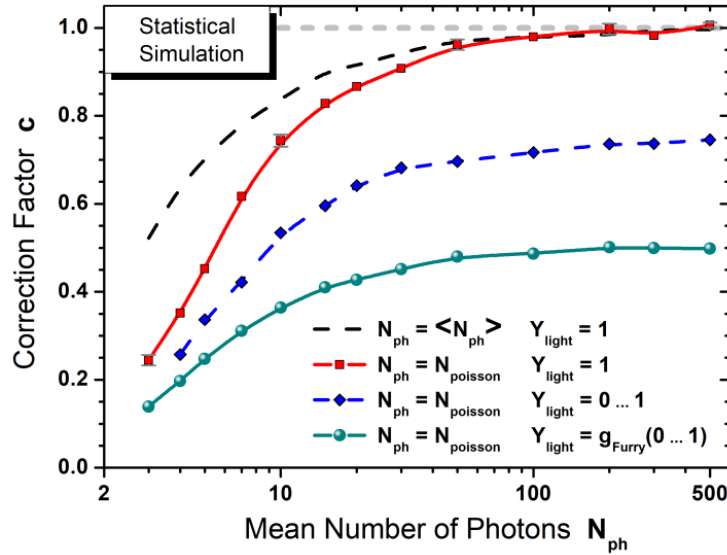
This means an effective number of photons is given by

$$N_{\text{eff}} = c \cdot N_{ph} \quad (3)$$

with $c=1$ for binary statistics at a large number of counts. In this case

$$N_{\text{eff}} = (\langle \sigma_d \rangle / \sigma_{\text{pos},d})^2 \quad (4)$$

At this point, we perform Monte-Carlo simulations with different boundary conditions to determine the value of c and to better understand the effective photon number under realistic experimental conditions. Fig. 9 displays the results of the simulations as function of the mean number of photons. For each event, a certain number of Monte-Carlo signals is generated with a Gaussian profile along an arbitrary coordinate. The mean position p_d of the event and the corresponding event width σ_d is then computed and stored. For each data point, 10,000 independent events have been considered for calculation of the mean width $\langle \sigma_d \rangle$ of all events (the arithmetic mean of the standard deviation for each distribution) and the width $\sigma_{\text{pos},d}$ of the bunch-position distribution. Since N_{ph} is known in the simulation, Eqs. 3 and 4 may be used to determine the correction factor c .



381

382

383

384

385

Fig. 9. Statistical correction factor c , given as a function of the mean photon number per bunch derived from simulations for different counting scenarios. Statistical uncertainties of the results are similar to the symbol sizes. See text for the definition of c .

386

387

388

389

390

391

392

393

394

395

The dashed gray line at the value of $c=1$ in Fig. 9 represents the limit of binary counting statistics. The long-dashed black curve corresponds to the numerical solution of the simple binary case, discussed above. Specifically at low photon numbers, the simulations show a significant drop below $c=1$. In an effort to understand the low value of c , we have checked modified computation schemes. It turns out that two modifications are meaningful. If we replace the so-called biased sample variance (normalized simply by N_{ph}) by the corrected sample variance (the so-called unbiased estimator of the population variance, normalized by $N_{ph}-1$) and if we average the *variance* over all events instead of the averaging the *standard deviations*, we reach $c=1$, down to very low photon numbers. In the experiment, however, we don't know the true photon number from the outset. Another problem is any uncertainty of a single event would have a larger influence on the variance than on the standard deviation. Thus, we did not adjust the evaluation procedure in the simulation.

396

397

398

399

400

Considering Poisson statistics for the given number of photons per event, we compute the square symbols with the underlying smoothed red curve. The resulting c is smaller than for constant photon numbers. Even for photon numbers exceeding 10, where Poisson distributions and Gaussian distributions are similar, there is a clear deviation from the black dashed curve. Thus, the width of the photon-number distribution determines the reduction of c . A large photon number in one event has the same influence on the result as a small photon number in another event. This leads to an effective reduction of the mean photon number and to a corresponding reduction of c .

401

402

403

404

405

406

407

408

409

410

411

In the streak camera, electrons are amplified at the end of the vacuum tube by a stochastic electron-avalanche multiplication process. After acceleration of the emerging electrons onto a phosphor screen, light is generated and detected with a CMOS camera. These last two steps yield an output signal roughly proportional to the electron intensity after the MCP. The MCP, however, generates a stochastic variation of the multiplied electron yield. Thus, data acquisition with the streak camera yields analog pixel values that have no one-to-one relation to a specific single-photon signature. Neither the number of active pixels nor the detected light signal may directly be converted into well-defined binary photon coordinates. The effect of a test-intensity variation on the simulation is shown by the diamond symbols (blue dashed curve), where each random photon coordinate is weighted by a homogeneous random distribution of the light intensity including primary Poisson statistics. The weighting leads to a clear reduction of c for all photon numbers. Large weighting factors reduce the influence of photon signals with small weights. This effect leads to an effective photon-number reduction as well.

412

413

414

415

416

417

Finally, we have used a statistical distribution obtained from the Furry function [37] that describes the output-pulse-height spectrum of single MCP electron-multiplication stages. The power factor that determines the specific shape of the pulse-height spectrum was fitted to single-stage MCP results published for a previous Hamamatsu streak-camera version [38]. Note that the fitted power factor is somewhat uncertain, since it should depend on the type of MCP and on the applied voltage for the avalanche multiplication. The lowest curve through the olive sphere symbols includes the effect of the MCP multiplication statistics, in addition to the Poisson statistics of the primary photon numbers per event.

418 There are many MCP pulses with very low output signal and a few with very high output signal. This suppresses the
 419 influence of low-intensity signals significantly and reduces the effective photon-number correspondingly.

420 With our qualitative and quantitative understanding of the statistical correction factor c (lower curve in Fig. 9), we
 421 can compute the detected number of photons from Eqs. 3 and 4. The underlying experimental variance parameters (σ_d)
 422 and $\sigma_{pos,d}$ are given in Figs. 7 and 8 together with their uncertainties. The square of their ratio yields N_{eff} , and the deviation
 423 by c leads to the detected number of photons N_{ph} . These results are presented in Table 1. The 1st line for the hori-
 424 zontal evaluation of the camshaft bunch in Table 1 corresponds, e.g., to the sub-plots a) and b) in Fig. 7. For this bunch,
 425 the results evaluated independently for the horizontal direction x and for the longitudinal bunch direction t , agree to
 426 within two standard deviations. The camshaft evaluation for the longitudinal direction agrees perfectly with the direct
 427 hit-counting results. This is also true for the PPRE evaluation along the longitudinal direction. This proves the success
 428 of our method of the statistical analysis of streak-camera snapshots.
 429

Bunch Type	Statistical Streak-Camera Evaluation				Direct Counting
	Direction	N_{eff}	c	N_{ph}	
Camshaft	Horizontal	96.9	0.500	194±10	219±6
	Longitudinal	109.4	0.501	219±10	
PPRE	Horizontal	30.4	0.482	—	162±4
	Longitudinal	80.8	0.496	162±11	

Table 1. Evaluation of the measured horizontal and longitudinal peak properties of the snapshot data series for the camshaft and PPRE bunches (see text). The absolute detected photon numbers N_{ph} per turn and bunch (uncertainties do not include the systematic error of the MCP pulse-height distribution) are derived from the statistical analysis of variance properties for both directions and from direct counting of measured photon blobs for both types of bunches. For the horizontal PPRE evaluation, N_{ph} is not stated, because non-statistical effects do influence N_{eff} (see text).

430

431 The only result that appears to be inconsistent with the statistical approach stems from the horizontal PPRE evalua-
 432 tion. N_{eff} determined for this case is significantly lower than N_{eff} for the longitudinal coordinate of the same bunch. It is
 433 also lower than expected from the 162 photons determined via direct counting of photon hits. This result is expected as
 434 we performed the investigation in order to search for horizontal position fluctuations of an excited bunch. Using N_{eff}
 435 =80.8, from the longitudinal analysis, as well as Eqs. 2 and 3 we estimate a pure statistical broadening of $\sigma_{pos,x}^{(stat)} =$
 436 $\langle \sigma_x \rangle / \sqrt{80.8} = 4.09$ pxl, about 39% below the measured position fluctuation of $\sigma_{pos,x}^{(meas)} = 6.67$ pxl. Thus, there is a
 437 residual horizontal orbit motion $\sigma_{pos,x}^{(orbit)}$ over many turns. Assuming that Gaussian distributions yield a reasonable de-
 438 scription, the orbit jitter may be derived using standard Gaussian deconvolution so that

$$439 \sigma_{pos,x}^{(orbit)} = \sqrt{\sigma_{pos,x}^{(meas)2} - \sigma_{pos,x}^{(stat)2}} = 5.27 \text{ pxl.}$$

440 This means that the major part of the horizontal beam-center fluctuation observed with the streak camera is due to a
 441 motion of the electron orbit in the ring and not due to statistics. However, this orbit fluctuation is just 14% of the hori-
 442 zontal absolute beam size, consistent with the experimental PPRE requirements. Further tests of this method with dif-
 443 ferent photon intensities and variable excitation strength of the PPRE bunch are ongoing.

444 Here we have shown that a statistical snapshot analysis can yield absolute detected photon numbers, in good agree-
 445 ment with counted photon hits and with the expected number of photons, derived from the initial light power and beam-
 446 line-transmission properties. Furthermore, this method enables determining bunch-measurement fluctuations quantita-
 447 tively in any direction. Judging from the uncertainties found in this work, determination of position fluctuations at a
 448 level of 5% of the width of a peak structure appears possible even for snapshots with only about 100 hits per peak.

449

2.5. Accurate trigger signals

450 Both the FSC as well as the ICCD operation are strongly dependent on the fidelity of the trigger signals. Thus, we
 451 have determined the timing jitter of a variety of different timing signals using a Signal-Source Analyzer (SSA, for the
 452 frequency range f_j from 1 Hz to 20 MHz) and a fast Mixed-Signal Oscilloscope of type Tektronix MSO 71254C (maxi-
 453 mum effective bandwidth of $f_j = 1$ kHz to 12.5 GHz at 100GS/s). For the SSA we use the differential phase-noise signal
 454 to determine the jitter for a specific frequency range. Contrary, for the MSO we may restrict the bandwidth correspond-
 455 ingly using the internal adjustable digital band-pass filter and select a maximum time range for the data stream. Finally,
 456 we perform a more accurate offline analysis for large MSO signal-data sets (via independent curve-fitting at each stored
 457 signal period) and correct for the internal trigger/acquisition jitter of 270/100 fs. Dependent on the considered frequency
 458 interval, we have to add two partial timing-jitter values obtained with both systems (SSA and MSO).

459 The 500-MHz RF transmitted from the BESSY II Master Oscillator (MO) via fiber cable to the diagnostic platform
 460 yields an rms timing jitter of 700 fs as determined with the Oscilloscope (sensitivity range: 1 MHz to 1 GHz). Depend-
 461 ent on the specific data-acquisition mode, different trigger-frequency ranges determine the all-over jitter of the system.
 462 These modes are

- 463 • mode 1: single-trigger single-shot FSC acquisition (single-exposure time $\leq 1 \mu\text{s}$),
- 464 • mode 2: continuous trigger single-shot FSC-acquisition (short-time exposure $\cong 1 \text{ ms}$),
- 465 • mode 3: time-integrated analog or photon-counting FSC-acquisitions (exposure $\cong 1 \text{ s}$),
- 466 • mode 4: time-integrated ICCD-acquisition (exposure time $\cong 100 \text{ ms}$).

467 The fast-scan axis of the FSC requires a 125-MHz signal derived from the MO after division by 4. The FSC includes a
 468 M10911-01 synchroscan unit that limits the accepted synchronous frequency range to $125 \pm 0.2 \text{ MHz}$. This bandwidth
 469 determines the upper f_j value for the data-acquisition modes 1 to 3. Thus, phase-locking leads to an optimum time reso-
 470 lution for the short exposure time at mode 1, since the bandwidth for accepting external noise should be zero. This in-
 471 trinsic time resolution is $(0.88 \pm 0.18) \text{ ps}$ FWHM ($\sigma \cong 0.37 \text{ ps}$ rms) for mode 1 [4], limited only by the point-spread func-
 472 tion and the internal electronic and electron-optical noise of the FSC system.

473 Using an improved version of the ray-tracing program RAY-UI [17], we have determined the time resolution for the
 474 transport of visible light from the bending magnet onto the FSC cathode. A photon-transport jitter of 0.9 fs rms follows
 475 from simulations accounting for the bent photon-source distribution including lateral electron-beam widths and angular
 476 divergences as well as roughness and slope errors of the mirrors. Thus, photon transport inside the evacuated beamline
 477 does not contribute significantly to the overall FSC time resolution. Considering position-dependent path-length varia-
 478 tions and wavelength dispersion of the wedged exit window (0.5° wedge angle), we estimate a corresponding timing
 479 jitter of 0.39 ps FWHM. Thus, we expect an all-over time resolution of 0.96 ps FWHM for the current FSC configura-
 480 tion without beam splitters in the optical system. Consequently, we require an electronic jitter below 0.5 ps FWHM in
 481 the external timing circuits for modes 2 and 3.

482 In the following, we compare the jitter of the local 500-MHz signal (**MO**) with the outputs of three low-jitter fre-
 483 quency converters that deliver the 125-MHz for modes 2 and 3, as well as 1.25-MHz for mode 4, by considering the
 484 mode specific input-bandwidth limits. The three frequency converters are

- 485 • the **Hamamatsu** standard FSC device (RF Countdown Unit C10658-02 for modes 1 to 3),
- 486 • an **Optronis** LJFD/H4 frequency divider (for modes 1 to 3) or a divider chain for mode 4,
- 487 • a **HZB** internal development for mode 4, based on the AD9513 chip by Analog Devices.

488 For the different data-acquisition modes in Table 2, the Optronis unit yields the least noise contributions. During the
 489 write-up of this paper, we have thus switched to a new Optronis 500-MHz LJFD/H4 frequency divider for the fast-
 490 timing synchronization of the FSC. All data published herein, however, have been taken with the Hamamatsu unit.

491 For any bunch-selective measurement, a well-defined revolution-trigger signal at 1.25-MHz is necessary, correspond-
 492 ing to 500-MHz divided by the fixed number of 400 buckets within a complete filling pattern (see mode 4 in Table 2).
 493 For the FSC, the all-over timing jitter should be small compared to $\pm 50 \text{ ps}$, as this corresponds to a single CCD pixel for
 494 the smallest slow-scan time-range (100 ns) of the streak camera. For the high resolution ICCD, the revolution-trigger
 495 jitter should even be below $\pm 5 \text{ ps}$, in order to match the expected internal ICCD timing jitter.

496

	mode 2	mode 3	mode 4
	$f_j = 1 \text{ kHz} - 0.2 \text{ MHz}$	$f_j = 1 \text{ Hz} - 0.2 \text{ MHz}$	$f_j = 10 \text{ Hz} - 1 \text{ GHz}$
MO	20 fs	135 fs	1.04 ps
Hamamatsu	260 fs	1160 fs	-
Optronis	50 fs	145 fs	2.2 ps
HZB	-	-	2.6 ps

Table 2. External rms noise contributions delivered by different devices for specific data-acquisition modes (see above) of the FSC and the ICCD system and the related frequency ranges. The main information stems from the SSA, but the high-frequency components for mode 4 are taken from the MSO.

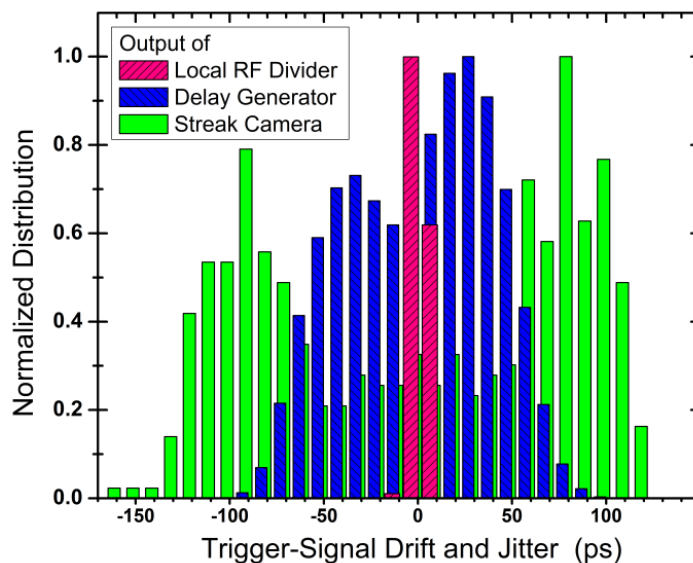
497

498 The standard BESSY 1.25-MHz revolution trigger (transmitted via fiber cable) shows a short-time jitter of $\sim 200 \text{ ps}$
 499 during some minutes of data-acquisition time and temperature drifts above 1 ns during 24 hours. These values are nei-
 500 ther acceptable for the FSC measurements nor for the planned ICCD experiments. Thus, we have tested two solutions for
 501 generating a local 1.25-MHz revolution trigger signal from the 500-MHz reference.

502 We have used an Optronis divider chain consisting of LJFD/H4, LJFD/H2, and LJFD/N, with $\sigma = 2.2 \pm 0.2 \text{ ps}$ (see Ta-
 503 ble 2) plus an additional long-time drift of 4.1 ps during 24 hours of operation. Synchronization to the BESSY revolu-
 504 tion trigger is possible only for the last divider of the Optronis chain. In addition, we have also started an internal devel-

505 opment in our research center by using divider-evaluation boards of the type AD9513 by Analog Devices. Here, we
 506 have measured $\sigma=2.6 \pm 0.3$ ps (see Table 2). The long-time temperature drift of the test unit is currently 30 ps and re-
 507 synchronization is still missing, but both will be improved soon. Thus, already now we have two acceptable solutions
 508 for a precise revolution trigger. The final decision for one of the systems will depend on the achieved performance of
 509 the ongoing in-house development, as this system will include some advantages over the commercial one (complete re-
 510 synchronization and multiple output frequencies).

511 Fig. 10 displays the measured jitter at three different points of the FSC trigger system for the slow axis. The pink
 512 bars represent the Optronis divider chain for the revolution-trigger (the peak width is dominated by the binning size of
 513 10 ps). The blue bars represent the output jitter of the DG-645 digital delay generator from Stanford Research Systems.
 514 Without steady re-synchronization of the divider chain, this distribution becomes narrower ($\sigma= 25$ ps instead of 45 ps,
 515 as in the plot). The green bars display the drift and jitter of the analyzed FSC peak positions in the horizontal direction.
 516 This bi-modal distribution corresponds to about ± 1 pixel on the camera chip. It is related to the temperature drift over
 517 24 hours and the green distribution would be very close to the blue one for measurements below 1 hour.
 518



519
 520 **Fig. 10.** Long-time investigation (over about 24 hours) of jitter and drift in the horizontal FSC trigger systems.
 521

3. FURTHER DEVELOPMENTS

3.1. Button BPM design and signal shaping

524 The BESSY II fill-pattern monitor and also the feedback system based on Beam-Position Monitors (BPMs) feature
 525 bunch-resolved operation. For constant bunch filling the BPMs deliver high quality data. An observed signal ringing in
 526 the BPM output, however, causes different problems. There are changes of the signal shape along the bunch train due to
 527 long-time interference of the unwanted ringing. Furthermore, misreading of the beam position of low-charge bunches
 528 following a high-charge bunch seems to be unavoidable. In order to mitigate signal-ringing effects, three distinct solu-
 529 tions are being investigated.

- 530 • The development of new button-type BPMs [40] leads to reduced signal ringing by proper choice of an opti-
 531 mized structure. Tapered internal structures lead to a reduced reflection coefficient. By the choice of geometry
 532 and materials, the cutoff frequency is increased and trapped high-Q modes driving long-lasting oscillations may
 533 be suppressed.
- 534 • Analog signal mixing with passive self-compensation has been tested successfully [4]. Adding a reflected phase-
 535 inverted and delayed signal to the primary signal acts like a short-cut for low signal frequencies. Furthermore, it
 536 reduces long-time oscillations at a fixed high frequency by a proper choice of delay time and reflection coeffi-
 537 cient.
- 538 • Use of additional low-pass filters suppresses unwanted frequency components in the GHz regime. Typical pas-
 539 sive Butterworth-type LC filters, however, produce multiple oscillations due to their logarithmic phase variation

540 at the upper stopband. These oscillations are circumvented by the use of Bessel-type filters that involve a linear-
541 phase response.

542 3.2. Trigger-free bunch-length measurements

543 All FSC timing results are related directly to the fast 125-MHz trigger signal. Technically, the device performance re-
544 lies on the stability of the electronic trigger signal. The same holds true for all other time-critical elements of the elec-
545 tron ring. Physically, each bunch may oscillate longitudinally within its bucket, being not stable w.r.t. a trigger signal.
546 Particularly for low- α or low-current operation, long integration times are required to obtain a reasonable statistical
547 accuracy. Under this condition, the long-term jitter and drift of all timing systems can limit the measurement accuracy.
548 Specifically, there is no simple direct way to distinguish between an intrinsically broadened and an oscillating compo-
549 nent of a bunch. Therefore, we are going to investigate three additional methods for trigger-free bunch-lengths determi-
550 nation that are appropriate for quantitative investigation of the intrinsic structure of short bunches.

- 551 • Our timing beam line yields a high radiation power (exceeding 1 mW for visible light). Thus, second-harmonic
552 autocorrelation with a nonlinear BBO (β -Barium Borate) crystal for type-I phase-matching and a single-photon
553 camera is envisaged. Splitting the light into two paths should yield the self-convoluted time structure as a func-
554 tion of the setting of our precision delay stage [5].
- 555 • For weak photon sources, coincident two-photon detection enables intensity interferometry via 4th-order ampli-
556 tude (2nd-order intensity) correlations using two arms of an optical interferometer [41]. Similar as for method 1,
557 the variation of the 2-photon yield shall be measured as a function of the optical delay [5].
- 558 • A simple extension of our experimental capabilities is the use of the optical delay table for producing close dou-
559 ble pulses of individual bunches. The mean position of one peak may be used to define the trigger condition for
560 the second pulse, similar as in previous reference-peak methods. [42,43] Using Fig. 9 and Eq.2 of the quantita-
561 tive snapshot-analysis of section 2.4., one may estimate that a minimum of 10 photons per pulse are necessary to
562 reach a sub-ps resolution in a trigger-free measurement.

564 4. CONCLUSION

565 Many developments are running in parallel to improve the electron-beam diagnostics at BESSY II to reach robust
566 bunch-selective monitoring of beam-position, beam size and trigger-free timing at BESSY II. We have reached an all-
567 over time resolution (including streak camera, light dispersion and trigger jitter) of about 1.5 ps FWHM with averaging
568 over a few minutes even at low beam currents [44]. This operation at beam currents of only 0.0003 mA per bunch
569 proves the high sensitivity of the setup, due to large source opening angles and high beam-line transmission. For the
570 typical BESSY II ring current, however, we can use a band-path filter to reduce the dispersion at the beam splitters and
571 the vacuum outlet-window. Under this condition, we should come close to our measured (dynamic) camera time-
572 resolution of 0.88 ps FWHM [4], specifically for low data acquisition times (between single shot and a few ms). Com-
573 parison of FSC peak-intensities with data from the BESSY-II bunch-filling monitor indicates a large dynamic range of
574 the streak-camera and thus, a good signal-to-noise ratio.

575 By opening the horizontal slit (in the slow-scan direction), the streak-camera system may be switched from optimum
576 bunch separation to the 2D operation mode. Since summer 2019, such measurements are a part of regular machine
577 commissioning, used for testing the size and stability of the PPRE bunch. Several types of bunch-resolved 2D mea-
578 surements of size and/or position dependencies at specifically excited electron buckets or also Transverse Resonance
579 Island Buckets (TRIBs, see [45]) have been performed successfully. Lateral interferometry with π -polarized light [6,16]
580 has been proven as a new feature of 2D streak measurements [18]. First measurements with the improved optical relay-
581 line system show very promising 2D-interferometry results.

582 A statistical treatment of the 2D structures measured with the fast streak camera shows that absolute photon numbers
583 may be obtained from single-turn single-bunch properties. This snap-shot method works in principle also for strongly
584 overlapping photon blobs, where direct counting is not possible. The same method yields accurate quantitative results
585 for orbit instabilities well below the detected spot size.

586 The interferometric double-slit beam-size determination has passed many tests successfully. Currently, a new beam-
587 line for transverse interferometry is being finalized and first light has been obtained during the final write-up of this
588 paper. After first commissioning, the setup will be completed with an ICCD camera for bunch-selective operation. Here
589 we will average the ICCD illumination for 10000 to 20000 turns and expect sufficient statistical accuracy for bunch-
590 selective interferometry with high lateral precision. Other diagnostic methods are still in the evaluation phase.

591
592
593
594

APPENDIX

Here, we compare our streak-camera system with other multi-dimensional systems. First, note that none of these systems detects full (correlated) 3D bunch structures. Instead, they all detect different 2D distributions for time vs. each of the two lateral directions. Most systems enable also x vs. y detection (for large bunch separations), e.g., by reduction of the streaking effect at significantly lower streaking speeds [28]. With our high-repetition-rate sweeping electronics, we may use the latter method for the short bunches of the low- α mode, at the lowest timing resolution and by opening the streak-camera entrance-slit completely. Alternatively, however, x vs. y detection can be performed directly with the fast gating ICCD (see section 2.2 for ICCD parameters). For comparison, we have selected two representative types of 2D streak systems.

- A pioneering work has been presented by Edouard Rossa in 1994 for the LEP collider at CERN [26,27]. This system is optimized for a series of single-bunch operations, where two projected 2D structures (t/x and t/y) are measured simultaneously for an electron bunch in addition to a positron bunch in the collider.
- In 2015, Switka and Hillert [29] have published papers on a system that has been installed at ELSA. It is improved over the Rossa system regarding the relay line and the streak-camera properties. It allows for synchroscan operation, appropriate for bunch-train detection of two projected 2D structures (t/x and t/y) at a bunch separation of 4 ns (every 2nd bunch).

Both of these systems involve parallel measurement of t/x and t/y distributions, whereas our system may be switched between both settings (it takes about 10 minutes). This appears to be a disadvantage, but our system is able to detect complete bunch trains (odd and even bunches at a bunch separation of 2 ns) in the synchro-scan mode. Thus, we do not need to investigate odd and even bunch positions separately. For the x/y conversion, the other two systems make use of a so-called Dove prism, which, however, involves a significant temporal broadening of about 7 ps [29]. Our scheme is nearly dispersion-free, since such a Dove prism is not necessary.

Thus, all three systems detect and store 4 different types of information along the streaking direction, but with different intentions. Our system is optimized for dense and complex filling patterns, where neighboring bunches have to be visualized with extremely high position and time resolution. As it may be extracted from the subsequent table, our system involves the highest sweeping rate (1000 full sweeps per second), the lowest timing jitter, the best total time-resolution and a good spatial resolution. The large opening angles (edge-to-edge 20 mrad horizontally \times 5 mrad vertically) of the first focusing mirror lead to a low diffraction limit and also to a high photon flux that enables single-shot measurements even at bunch charges as low as about 10 pC.

2D System	Refs. 26 and 27	Ref. 29	This work
Streak-camera Type & company	ARP France	C10910 Hamamatsu Japan	Mod. ⁽¹⁾ C10910 Hamamatsu
Streak data-rate (Hz)	10 – 25	0 – 10	0 – 1000
Single-bunch Operation	X	X	X
Multi-bunch operation ⁽²⁾		X	X
Camera time-resolution (ps)	≤ 6	$\cong 1$	0.88 (see [4])
Trigger jitter (ps)	≤ 5	2.7 ⁽³⁾	≤ 0.4 ⁽⁴⁾
System time-resolution (ps)	≤ 10 ⁽⁷⁾	$\cong 7$	≤ 1.5 ⁽⁵⁾
point-spread function ⁽⁶⁾	1.8 px $\cong 15 \mu\text{m}$	4.1 px = 14 μm	4.1 px = 14 μm
Spatial geometrical beam-size resolution (μm)	$\cong 1000$ ⁽⁷⁾	$\cong 400$ ⁽⁷⁾	H: 180 V: 210 ⁽⁸⁾

TABLE 3. Technical specifications of the three different 2D-streak-camera systems. FWHM values are stated for all widths/resolution data. The vertical beam-size is denoted by V and the horizontal direction by H. Where not given explicitly, the FWHM values have been extracted indirectly from published statements or published plots.

- 631 (1) Streak camera with mirror based entrance-optics A6856 and modified dual time-base unit M10916-01 with a maximum repeti-
632 tion rate of 1-kHz, specifically designed for our 2D system.
633 (2) System designed and tested at 500-MHz bunch-train repetition.
634 (3) Filtered Hamamatsu frequency divider C10658-02, see table 2 (mode 3).
635 (4) Filtered Optronis frequency divider, see table 2 (mode 3).
636 (5) Recently verified experimentally for BESSY II bunches in a negative low- α mode at extremely low beam currents [44].
637 (6) The given pixel value at the CCD/CMOS detector corresponds to the stated width at the entrance cathode of the streak camera.
638 (7) Estimated from the corresponding publications.
639 (8) The vertical peak resolution varies between 130 and 280 μm (depending on filter and polarization settings) and is thus close to
640 Abbe's 1D-diffraction limit (170 μm) of light. Incoherent ray-tracing results [17] including roughness and slope errors of all
641 mirrors yield similar data (160 μm horizontally and 280 μm vertically). More accurate diffraction simulations including rough-
642 ness and slope errors are in preparation [46].
643
644

645 ACKNOWLEDGEMENTS

646 This Work is supported by the German Bundesministerium für Bildung und Forschung, Land Berlin and grants of the
647 Helmholtz Association. We acknowledge vacuum- and beamline-developments as well as motorization by Ch. Kalus, R.
648 Fleischhauer and O. Pawlizki. Furthermore, we acknowledge the support for specification and testing of various cus-
649 tom-made mirrors by F. Siewert and J. Buchheim, the development of the local revolution trigger by B. Namaschk, the
650 improved ray-tracing code by P. Baumgärtel as well as helpful discussions with R. Mitzner and K. Holldack on different
651 subjects related to this work.
652

653 References

- 654 [1] A. Jankowiak *et al.*, "The Bessy VSR Project for Short X-Ray Pulse Production", in *Proc. 7th Int. Particle Accelerator Conf. (IPAC'16)*,
655 Busan, Korea, May 2016, pp. 2833-2836. doi:10.18429/JACoW-IPAC2016-WEPOW009.
656 [2] A. Jankowiak *et al.*, eds., "Technical Design Study – BESSY VSR", Helmholtz-Zentrum Berlin für Materialien u. Energie GmbH, Germany,
657 2015. doi: 10.5442/R0001.
658 [3] G. Wuestefeld, A. Jankowiak, J. Knobloch, and M. Ries, "Simultaneous Long and Short Electron Bunches in the BESSY II Storage Ring", in
659 *Proc. 2nd Int. Particle Accelerator Conf. (IPAC'11)*, San Sebastian, Spain, Sep. 2011, paper THPC014, pp. 2936-2938.
660 [4] G. Schiwietz, J.-G. Hwang, M. Koopmans, M. Ries, A. Schällicke, "Development of the Electron-Beam Diagnostics for the Future BESSY-VSR
661 Storage Ring", *J.Phys.: Conf.Series* **1067**, 072005, 2018.
662 [5] T. Mitsuhashi and M. Tadano, "Measurement of Bunch Length using Intensity Interferometry", in *Proc. 8th European Particle Accelerator
663 Conf. (EPAC'02)*, Paris, France, Jun. 2002, paper THPR110, pp. 1936-1938.
664 [6] J. Breunlin, Å. Andersson, N. Milas, Á. Saá Hernández, V. Schlott, "Methods for measuring sub-pm rad vertical emittance at the Swiss Light
665 Source", *Nucl. Instrum. Meth.* **A803**, p.55–64, 2015.
666 [7] T. Naito, T. Mitsuhashi, "Very small beam-size measurement by a reflective synchrotron radiation interferometer", *Phys.Rev. ST Accel-
667 erators and Beams* **9**, pp. 122802, 2006.
668 [8] R. Müller, T. Birke, F. Falkenstern, H. Glass, P. Kuske, R. Ovsyannikov A. Schällicke, D. Schüler, and K. Holldack, "BESSY II Supports an Ex-
669 tensive Suite of Timing Experiments", in *Proc. 7th Int. Particle Accelerator Conf. (IPAC'16)*, Busan, Korea, May 2016, pp. 2840-2843.
670 doi:10.18429/JACoW-IPAC2016-WEPOW011.
671 [9] F. Siewert and J. Buchheim, private communication (2018 and 2019)
672 [10] M. Koopmans, P. Goslawski, J. G. Hwang, M. Ries, M. Ruprecht, and A. Schaelicke, "Status of a Double Slit Interferometer for Transverse
673 Beam Size Measurements at BESSY II", in *Proc. 8th Int. Particle Accelerator Conf. (IPAC'17)*, Copenhagen, Denmark, May 2017, pp. 149-
674 152. doi:10.18429/JACoW-IPAC2017-MOPAB032 .
675 [11] M. Koopmans, "Interferometric Beam Size Monitor for BESSY II", master thesis at Humboldt-Universität zu Berlin (2017).
676 [12] M. Koopmans *et al.*, "Application of the interferometric beam size monitor at BESSY II", in *Proc. 9th Int. Particle Accelerator Conf.
677 (IPAC'18)*, Vancouver, Canada, May 2018, pp. 2103-2106. <https://doi.org/10.18429/JACoW-IPAC2018-WEPAK009>. See refs. therein.
678 [13] G. Kube, "Review of synchrotron radiation based diagnostics for transverse profile measurements", in Proceedings of the 8th European
679 Workshop on Beam Diagnostics and Instrumentation for Particle Accelerators (DIPAC 2007), Venice, Italy (Elettra Sincrotrone, Trieste,
680 Italy, 2007), pp. 6–10. See <https://accelconf.web.cern.ch/d07/papers/moo1a03.pdf>
681 [14] T. Mitsuhashi, "Beam Profile and Size Measurement by SR Interferometer" in: Beam measurement (ed. by S. Kurokawa et al., pp. 399–427,
682 World Scientific 1999).
683 [15] M. Boland, J. Corbett, and T. Mitsuhashi, "Measurement of the Incoherent Depth of Field Effect on Horizontal Beam Size Using a Synchro-
684 tron Light Interferometer", in: Proceedings of IPAC2015 (2015), TUPWA001, pp. 1391–1393.
685 [16] Å. Andersson, M. Böge, A. Lüdeke, V. Schlott, A. Streun, "Determination of a small vertical electron beam profile and emittance at the Swiss
686 Light Source", *Nucl. Instrum. Meth.* **A591**, p. 437–446 (2008).
687 [17] P. Baumgärtel, P. Grundmann, T. Zeschke, A. Erko, J. Viefhaus, F. Schäfers, and H. Schirmacher, "RAY-UI: New features and extensions", *AIP
688 Conference Proceedings* **2054**, 060034 (2019); <https://doi.org/10.1063/1.5084665>; timing calculations have been performed with RAY-
689 UI version qwt.1119 downloaded from <https://hz-b.de/ray>.

- 690 [18] M. Koopmans *et al.*, "Vertical Beam Size Measurement Methods at the BESSY II Storage Ring and their Resolution Limits", in *Proc. 10th*
691 *Int. Particle Accelerator Conf. (IPAC'19)*, Melbourne, Australia, May 2019, pp. 2491-2494. doi:10.18429/JACoW-IPAC2019-WEPGW012.
- 692 [19] K. Holldack, J. Feikes and W.B. Peatman, "Source size and emittance monitoring on BESSY II", *Nucl. Instrum. and Meth.* **A467-468**, 235-
693 238 (2001).
- 694 [20] J. Corbett, X. Huang, J. Wu, C.L. Li, T. Mitsuhashi, Y.H. Xu, W.J. Zhang, "Transverse beam profiling and vertical emittance control with a
695 double-slit stellar interferometer", in International Beam Instrumentation Conference (IBIC2016), Barcelona, Spain, 2016, paper
696 MOPG70. See also Chunlei Li, "Characterization of Field Polarization and Spatial Coherence in a Diffraction-Limited Visible Synchrotron
697 Radiation Beam", PhD thesis at East China University of Science and Technology (2017).
- 698 [21] L. Torino, U. Iriso, "Beam shape reconstruction using synchrotron radiation interferometry", in International Beam Instrumentation
699 Conference (IBIC2016), Barcelona, Spain, 2016, paper WEBL03.
- 700 [22] G. Trad, E. Bravin, A. Goldblatt, S. Mazzoni, F. Roncarolo, T. Mitsuhashi, "Beam size measurements using interferometry at LHC", in Inter-
701 national Beam Instrumentation Conference (IBIC2016), Barcelona, Spain, 2016, paper WEBL02; and references therein.
- 702 [23] L. Torino, "Longitudinal and transverse beam diagnostics using synchrotron radiation at ALBA", PhD thesis at Università di Pisa (2017).
- 703 [24] S.T. Wanga, R. Holtzapple, D.L. Rubina, "Single-shot beam size measurements using visible-light interferometry at CESR", *Nucl. Instrum.*
704 *Meth.* **A847**, 34-41 (2017).
- 705 [25] A.S. Fisher, M. Petree, R. Kraus, Y. Au, and B. Chan, "Turn-by-Turn Imaging of the Transverse Beam Profile in PEP-II", SLAC-PUB-11851,
706 Presented at the 12th Beam Instrumentation Workshop (BIW06), 2006, Fermilab, Batavia, IL/USA.
- 707 [26] E. Rossa, C. Bovet, L. Disdier, F. Madeline, J.-J. Savioz, "Real Time Measurement of Bunch Instabilities in LEP in three Dimensions using a
708 Streak Camera", EPAC Conference Proceedings, Vol.1, 144 (1992).
- 709 [27] Edouard Rossa, "Real Time Single Shot Three-Dimensional Measurement of Picosecond Photon Bunches", AIP Conference Proceedings
710 **333**, 148 (1995).
- 711 [28] Bingxin Yang, "Streak Camera 101: Visualizing Charged-Particle Beam Dynamics", AIP Conference Proceedings **868**, 124 (2006).
- 712 [29] M. T. Switka and W. Hillert, "Preserving Information of the Three Spatial Electron Beam Dimensions in One Streak Camera Measure-
713 ment", in *Proc. 6th Int. Particle Accelerator Conf. (IPAC'15)*, Richmond, VA, USA, May 2015, pp. 144-146, doi:10.18429/JACoW-IPAC2015-
714 MOPWA02; see also references therein.
- 715 [30] K. Holldack, private communication (2014) and E. Giangrisostomi, R. Ovsyannikov, F. Sorgenfrei, "LowDosePES: the low-dose photoelec-
716 tron spectroscopy end-station at the PM4 beamline at BESSY II", *Journal of large-scale research facilities JLSRF* **4**, A130 (2018), and ref-
717 erences therein, doi: <http://dx.doi.org/10.17815/jlsrf-4-114>.
- 718 [31] G. Schiwietz, M. Beye, D. Kühn, and G. Xiao; "The retarding Bessel-Box—An electron-spectrometer designed for pump/ probe experi-
719 ments", *Journal of Electron Spectroscopy and Related Phenomena* **203**, 51-59 (2015, DOI:
720 <http://dx.doi.org/10.1016/j.elspec.2015.06.011>).
- 721 [32] G. Schiwietz, D. Kühn, A. Foehlich, K.Holldack, T.Kachel, and N.Pontius; "Laser-pump/ X-ray-probe experiments with electrons ejected
722 from a Cu(111) target: space-charge acceleration", *J. Synchrotron Rad.* **23/5**, 1158-1170 (2016, DOI:
723 <http://dx.doi.org/10.1107/S1600577516009115>). *ibid*; "Dynam-ics of Space-Charge Acceleration of X-Ray Generated Electrons Emit-
724 ted from a Metal Surface", *Journal of Electron Spectroscopy and Related Phenomena* **220**, 40-45, (2017, DOI:
725 <http://dx.doi.org/10.1016/j.elspec.2017.03.003>).
- 726 [33] K. Holldack, R. Ovsyannikov, P.Kuske, R.Müller, A. Schällicke, M. Scheer, M. Gorgoi, D.Kühn, T. Leitner, S. Svensson, N. Mårtensson,
727 A.Föhlich, "Single bunch X-ray pulses on demand from a multi-bunch synchrotron radiation source", *Nature Communications* **Vol.5**,
728 4010, 2014.
- 729 [34] J.-G. Hwang, M. Koopmans, M. Ries, A. Schällicke, R. Müller, "Analytical and numerical analysis of longitudinally coupled transverse dy-
730 namics of Pulse Picking by Resonant Excitation in storage rings serving timing and high-flux users simultaneously", *Nucl. Instr. and*
731 *Meth.* **A940**, 387, 2019.
- 732 [35] M. Kammerer, M. Weigand, M. Curcic, M. Noske, M. Sproll, A. Vansteenkiste, B. Van Waeyenberge, H. Stoll, G. Woltersdorf, C. Back & G.
733 Schuetz, "Magnetic vortex core reversal by excitation of spin waves", *Nature Communications* **2**, 279 (2011), doi:
734 10.1038/ncomms1277.
- 735 [36] A. Bisig, M. Stärk, M.-A. Mawass, C. Moutafis, J. Rhensius, J. Heidler, F. Büttner, M. Noske, M. Weigand, S. Eisebitt, T. Tyliczszak, B. Van
736 Waeyenberge, H. Stoll, G. Schütz and M. Kläui, "Correlation between spin structure oscillations and domain wall velocities", *Nature*
737 *Communications* **4**, 2328 (2013), doi: <https://doi.org/10.1038/ncomms3328>.
- 738 [37] W. H. Furry, *Phys. Rev.* **52**, 569 (1937).
- 739 [38] T.Urakami, Y.Takiguchi, K.Kinoshita, and Y.Tsuchiya "Characterisation of photon-counting streak camera", *Proceedings Volume 0693*,
740 *High Speed Photography, Videography, and Photonics IV*; (1986), <https://doi.org/10.1117/12.936728>
- 741 [39] G. Schiwietz, U. Stettner, T. Zouros, N. Stolterfoht, "Investigation of the Impact- Parameter Dependence of Electrons Emitted in 30-, 100-,
742 350-keV H+ and 100-keV ³He²⁺ + Ar collisions", *Phys. Rev.* **A35**, 598-606 (1987).
- 743 [40] J.G. Hwang, G. Schiwietz, V. Duerr, D. Wolk, A. Schällicke, F. Falkenstern, M. Ries, "Preliminary test result of a new button-type beam posi-
744 tion monitor for BESSY II and BESSY VSR", presented at the 8th International Beam Instrumentation Conference (IBIC'19), Malmö,
745 Sweden, Sep. 2019, paper WEPP003.
- 746 [41] M. Baba, Y. Li, and M. Matsuoka, "Intensity Interference of Ultrashort Pulsed Fluorecence", *Phy. Rev. Lett.* **76**, 4697, (1996).
747 doi:10.1103/PhysRevLett.76.4697
- 748 [42] J. Larsson, "Ultrafast, jitter-free x-ray streak camera that uses single-photon counting", *Optics Letters* **26/5**, pp. 295-297 (2001),
749 <https://doi.org/10.1364/OL.26.000295>
- 750 [43] M. M. Murnane, H. C. Kapteyn, and R. W. Falcone, "X-ray streak camera with 2 ps response", *Appl. Phys. Lett.* **56**, 1948 (1990),
751 <https://doi.org/10.1063/1.103031>
- 752 [44] M. Ries, G. Schiwietz *et al.*, ongoing experimental campaign of pulse-length measurements for different ring conditions.

- 753 [45] P. Goslawski, A. Jankowiak, F. Kramer, M. Ries, M. Ruprecht, and G. Wuestefeld, "Transverse Resonance Island Buckets as Bunch Separation Scheme", in *Proc. 8th Int. Particle Accelerator Conf. (IPAC'17)*, Copenhagen, Denmark, May 2017, pp.3059–3062, doi:10.18429/JACoW-IPAC2017-WEPIK057
- 754
- 755
- 756 [46] M. Koopmans, PhD thesis at Humboldt-Universität zu Berlin, in preparation